ACS Energy LETTERS

http://pubs.acs.org/journal/aelccp

LETTER

Intermolecular Interactions in Hybrid Perovskites Understood from a Combined Density Functional Theory and Effective Hamiltonian Approach

Liang Z. Tan, Fan Zheng, and Andrew M. Rappe*

Department of Chemistry, University of Pennsylvania, Philadelphia, Pennsylvania 19104-6323, United States

ABSTRACT: We show how the complex molecular structure of hybrid perovskites can be understood simply in terms of a few important intermolecular interactions. We deduce structural rules and coupling constants from an extensive density functional theory study of the structural energy landscape of methylammonium lead iodide. We have generated an unbiased structure−energy database, taking into account the orientations of molecular dipoles and inorganic lattice distortions. Analysis of this database shows that room-temperature structures are heavily dominated by a few hydrogen bonding patterns and lattice distortion modes. The molecule−molecule interactions, mediated by lattice distortions and hydrogen bonding, are shown to favor alignment of molecules at right angles to each other. We develop an effective Hamiltonian which shows that this interaction drives the cubic−tetragonal phase transition, explaining the temperature dependence of the tetragonal distortion observed in experiment.

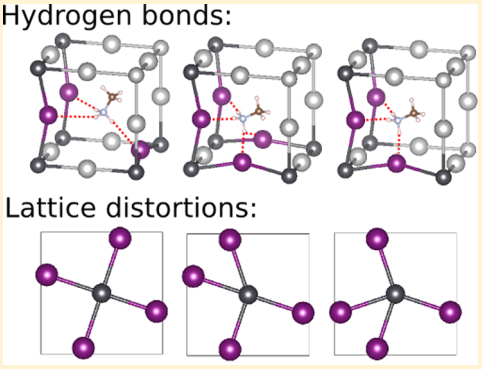

Hybrid halide perovskites have attracted significant attention in recent years because of their large and rising photovoltaic power conversion efficiency. In this class of materials, methylammonium lead iodide ($MAPbI_3$) in particular has emerged as an especially promising candidate, with reported power conversion efficiencies over 20%.[1−3] In addition, $MAPbI_3$ can be cheaply made using solution processing methods. Its cost, long carrier lifetimes,[4−6] and ideal band gap energy[7−11] make it promising as a next-generation solar material.

The perovskite structure of these materials consists of an inorganic PbI_3 lattice and a polar organic molecule at the A site. At room temperature, experiments have shown that the organic molecules display rotational motion.[12−14] At the same time, experiments[15,16] and molecular dynamics simulations[10,15,17−21] have shown that the PbI_3 lattice exhibits large amplitude motions with significant anharmonic character. Density functional theory (DFT) calculations have shown that the local electronic structure depends sensitively on the atomic structure, with band gap fluctuations,[22−24] Rashba effects,[25−32] and changes in electron−hole interactions[33] possibly appearing at the local scale. Therefore, it is important to understand the structural aspects of these hybrid organic−inorganic materials in order to explain the electronic properties that give rise to their high efficiency. Moreover, there is a lack of theoretical tools to decipher the complexity observed in computational simulations. The dipole−dipole coupling[13,34,35] widely used in the literature does not explain the propensity for molecules to align in "crossed" configurations, at 90° to each other.[36,37] In this work, to address these issues, we develop an effective model inspired by effective Hamiltonians in oxide perovskites,[38,39] building on first-principles calculations and identifying the dominant interaction modes of the organic molecules and the inorganic lattice. We show that the crossed configurations in fact play a crucial role in stabilizing the tetragonal phase and in the tetragonal−cubic phase transition.

Previous DFT calculations have been used to extract some low-energy structural models.[18,36,40,41] However, small unit-cell structures do not fully account for dynamical disorder at room temperature. Instead, the large number of degrees of freedom available to the molecules and the inorganic lattice and the presence of several small energy scales[13,42,43] suggest a complicated energy landscape with multiple competing energy minima. In the following, we derive an effective model which explains how this energy landscape arises from the interaction between charged polar molecules and inorganic lattice.

We start by constructing a first-principles structure−energy database for $MAPbI_3$ by calculating the DFT total energies for

Received: February 24, 2017
Accepted: March 28, 2017
Published: March 28, 2017

DOI: 10.1021/acsenergylett.7b00159
ACS Energy Lett. 2017, 2, 937−942

200 structural motifs. To obtain an unbiased sampling of the entire energy landscape, we initialize our structure−energy database with randomized structures. Each structure is initialized with the C−N axis of each methylammonium (MA) molecule directed along a random direction, and with the PbI_3 lattice in the undistorted configuration ($a^0a^0a^0$), with no rotations of PbI_6 octahedra. The angles of rotation of NH_3 and CH_3 tetrahedra about the C−N axis were separately initialized to random values, i.e., neither eclipsed nor staggered[36] H positions were assumed. These initial structures are then allowed to relax to local energy minima. The structures considered are constructed in a 2 × 2 × 2 supercell, using the lattice constants of the room-temperature tetragonal phase (a = b = 12.45 Å, c = 12.69 Å). We carry out these calculations using the PBE exchange-correlation energy functional[44] including van der Waals corrections[45,46] and norm-conserving pseudopotentials.[47,48] A 4 × 4 × 4 k-mesh and a 50 Ry plane-wave kinetic energy cutoff are used for self-consistent evaluation of the charge density. It was found that the MA molecules overwhelmingly relax to staggered configurations, with 93% of molecules having torsion angles within 60 ± 5°.

In $MAPbI_3$, hydrogen atoms on methyl and amino groups bond to iodine atoms, with the hydrogen atoms on amino groups displaying stronger hydrogen bonding due to the electronegativity of nitrogen. From our structure−energy database, we find that the average hydrogen bond length for amino groups is 2.76 Å, compared to 3.33 Å for methyl groups. Figure 1b shows that amino group hydrogen bonds are much shorter than the majority of methyl group hydrogen bonds, which is consistent with previous findings.[36,49,50] Each hydrogen atom in an amino group may form hydrogen bonds with one or more iodine atoms. Considering the distribution of bond lengths for each hydrogen atom, we find that the shortest bond for each hydrogen atom is typically 0.7 Å shorter than the next-shortest (Figure 1c). Therefore, most hydrogen atoms on the amino groups can be considered to have a single active H-bond. However, a small fraction of hydrogen atoms have two almost equidistant bonds, as can be seen from the bimodal distribution of bond lengths in Figure 1c. These statistics suggest a categorization of hydrogen bonding modes based on the shortest and second-shortest hydrogen bonds of the amino group. Considering the 12 iodine atoms in the cuboctahedral cage surrounding each MA molecule, all such hydrogen bonding modes can be enumerated by selecting the three or more I atoms located on the edges of the cubic cage (Figure 1a) which form the shortest hydrogen bonds with the amino group.

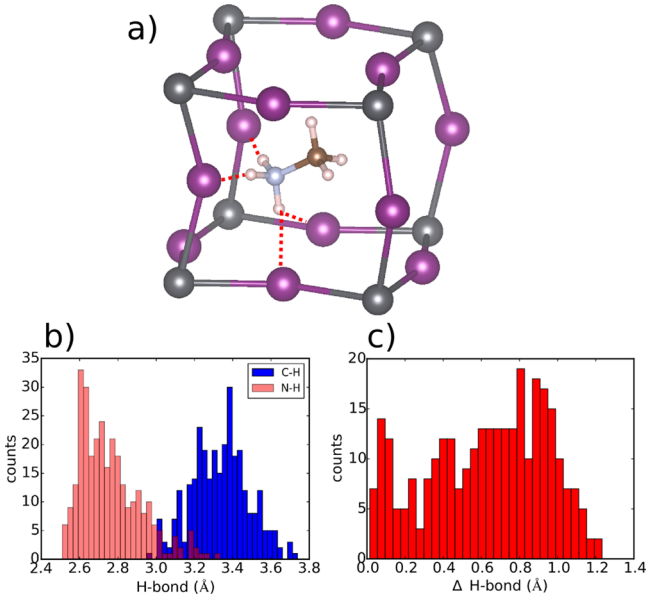

Figure 1. (a) Schematic of $MAPbI_3$ structure, showing MA molecule with hydrogen bonds (red, dashed) to iodine atoms, which move toward MA. (b) Distribution of hydrogen bond lengths, for amino (light red) and methyl groups (dark blue). (c) Distribution of the difference between shortest and second-shortest hydrogen bonds for each hydrogen atom in amine groups. The cluster with bond-length differences less than 0.1 Å indicates that some hydrogen atoms have strong H-bonds to two different iodine atoms.

We find that a few symmetry-inequivalent modes dominate the hydrogen bonding in our database. In Figure 2, we show the most common hydrogen bonding modes at different energies. We collect all hydrogen bonding modes present in structures with total energies within successive energy windows, considering modes related by rotations or reflections to be equivalent. The lowest-energy structures are entirely dominated by a single hydrogen bonding mode (H_A), which is consistent with the theoretically proposed molecular orientations for the low-temperature orthogonal phase.[50] At higher energies, more hydrogen bonding modes become available, but three in particular account for most of the database. Hydrogen bonding modes H_A and H_C involve all three amino hydrogen atoms each bonding to one primary iodine atom, while H_B involves four primary hydrogen bonds including one amino proton bonding

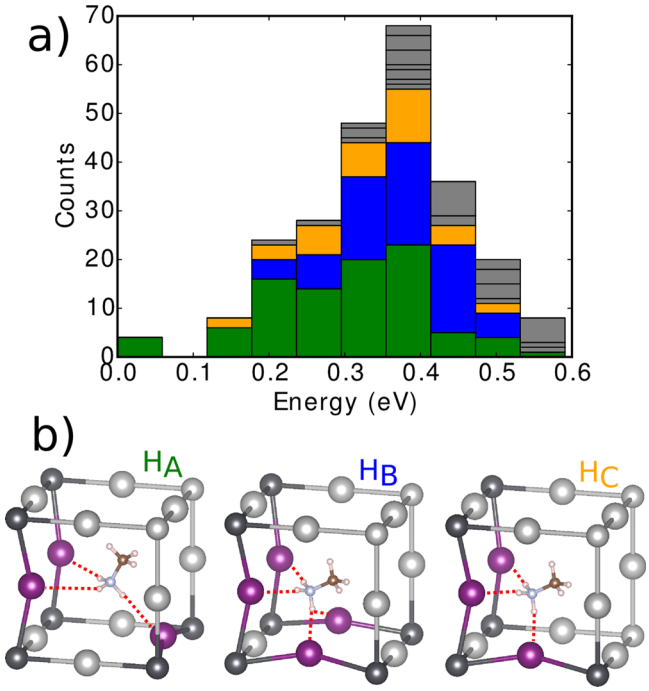

Figure 2. (a) Histogram of DFT total energies per 2 × 2 × 2 simulation cell and hydrogen bonding modes. Energies are referenced to the lowest-energy structure in the database. Colors indicate different hydrogen bonding modes: H_A (green), H_B (blue), and H_C (orange). Other modes are colored gray. (b) Schematic depictions of H_A, H_B, and H_C. Iodine atoms involved in hydrogen bonding are shown in dark color (purple).

DOI: 10.1021/acsenergylett.7b00159
ACS Energy Lett. 2017, 2, 937−942

strongly to two different iodine atoms (Figure 2b). The dominance of these three modes persists for the entire energy range. Other modes are possible at high energies but still account for only a small fraction of structures. In ref 51, a mode similar to H_B has been proposed as the major contributor to the hydrogen bonding network.

We also categorize the distortions of the inorganic lattice based on displacements of iodine atoms from high-symmetry positions. Considering that each iodine atom is displaced toward and forms hydrogen bonds with one of four adjacent MA molecules, we enumerate all possible lattice distortion modes for a PbI_6 octahedron by considering displacements of each iodine atom in one of these four directions. We consider distortions related by rotations and reflections to be equivalent. We note that this includes more distortion modes than Glazer's scheme,[52] because pure octahedral rotations and ferrodistortive displacements are both allowed here.

We find that only three symmetry-inequivalent distortion modes account for the majority of structures in our database, similar to the statistics for the hydrogen bonding modes. Mode L_A is the pure octahedral rotation mode, while modes L_B and L_C are a combination of octahedral rotations and ferrodistortive displacements, in that there are axes about which the I atoms do not form a pure rotation pattern around the central Pb atom (Figure 3). The fact that only three lattice distortion modes dominate the energy landscape suggests the presence of significant short-range order in $MAPbI_3$. To see this, we consider a hypothetical structural model where each I atom forms hydrogen bonds randomly to adjacent MA molecules and in an uncorrelated manner from other I atoms. Such a model predicts a wide distribution of possible lattice distortion modes, in sharp contrast to the distribution observed in our database. The presence of modes L_B and L_C shows that the nature of short-range order cannot be solely described by octahedral rotations. As with the hydrogen bonding modes, the lowest-energy structures are completely dominated by a single mode (L_A), while higher-energy structures allow more modes. In particular, the lattice distortions in the low-temperature *Pnma* orthorhombic phase are pure octahedral rotations ($a^+b^-b^-$).

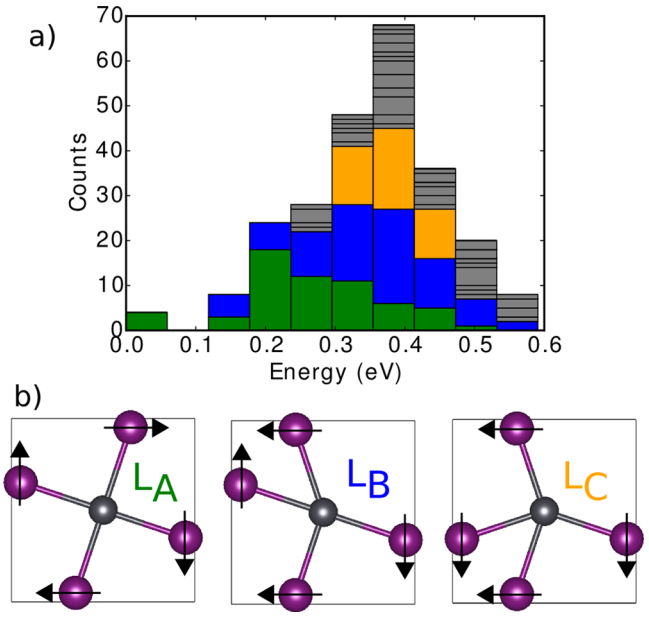

Figure 3. (a) Histogram of DFT total energies per 2 × 2 × 2 simulation cell and lattice distortion modes. Energies are referenced to the lowest-energy structure in the database. Colors indicate different lattice distortion modes: L_A (green), L_B (blue), and L_C (orange). Other modes are colored gray. (b) Schematic depictions of L_A, L_B, and L_C. Iodine (purple) and lead (gray) atoms are shown along a crystallographic axis. For all three modes, displacements about the other two crystallographic axes are pure rotations (as in L_A). Black arrows indicate displacement of iodine atoms away from high-symmetry positions.

The structural rules for hydrogen bonding ($\{H\}$) and for lattice distortions ($\{L\}$) derived above are interrelated, because hydrogen bonds form only from each MA to those iodine atoms displaced toward it. Together, these simple structural rules H_A, H_B, H_C, L_A, L_B, and L_C constrain the atomic structure of $MAPbI_3$. To see this, we take the lowest-energy modes L_A and H_A and find all structures with these modes in a 2 × 2 × 2 cell. That is, we consider all rotation patterns in a 2 × 2 × 2 cell and constrain each MA molecule to form hydrogen bonds consistent with H_A and the surrounding iodine atoms. By explicit enumeration, we find that there is a single rotation pattern, $a^+b^-b^-$, which accommodates these modes, leading to the space group (*Pnma*) of the orthorhombic phase. The higher-energy hydrogen bonding mode H_B can appear only with L_B and L_C, which are not pure octahedral rotations. There are multiple structures accommodating these higher-energy modes; for entropic reasons, they become available only at higher temperatures. This is in agreement with neutron diffraction experiments which have suggested the predominance of mode H_B at room temperature.[14]

To understand how these hydrogen bonding modes affect macroscopic structural properties, we develop an effective model Hamiltonian $H = H_{SR} + H_{LR}$ consisting of short-range (SR) and long-range (LR) interactions:

$$H_{LR} = \sum_{i,j} K\left(\frac{\vec{p}_i\cdot\vec{p}_j - 3(\hat{d}\cdot\vec{p}_i)(\hat{d}\cdot\vec{p}_j)}{r_{ij}^3}\right)$$
$$H_{SR} = \sum_{n.n.} g(p_i, p_j) \quad (1)$$

Here, the degrees of freedom of the model are the orientations of molecules $\vec{p}_i$; the distance between two molecules is r_{ij}, and the unit displacement vector between them is $\hat{d}$. Here, we focus on the room-temperature tetragonal phase, and the hydrogen bonding mode H_B is predominant in this phase. We take the molecular orientations $\vec{p}_i$ to be in one-to-one correspondence with a hydrogen bonding mode of type H_B with a particular orientation. For instance, the molecular orientation in Figure 1a is assigned the H_B mode of the orientation shown in Figure 2b. For simplicity, the molecules are taken to be oriented toward the faces ($\langle 100\rangle$ directions), as is expected for the tetragonal phase.[14] An effective interaction between the hydrogen bonds of adjacent unit cells is mediated by the sharing of iodines between hydrogen bonds of different unit cells or the displacement of iodine which inhibits hydrogen bonding in some unit cells in favor of others. This interaction is described by the SR term in our effective Hamiltonian, which we parametrize using the four most energetically favorable configurations of two MA molecules (p_i, p_j) with H_B modes in different orientations. We assign an energy $g(p_i, p_j)$ to the SR term for each of these configurations, with values of $g(p_i, p_j)$ given in Figure 4. We consider only these four interactions, and we consider only nearest-neighbor interactions because they are

DOI: 10.1021/acsenergylett.7b00159
ACS Energy Lett. 2017, 2, 937–942

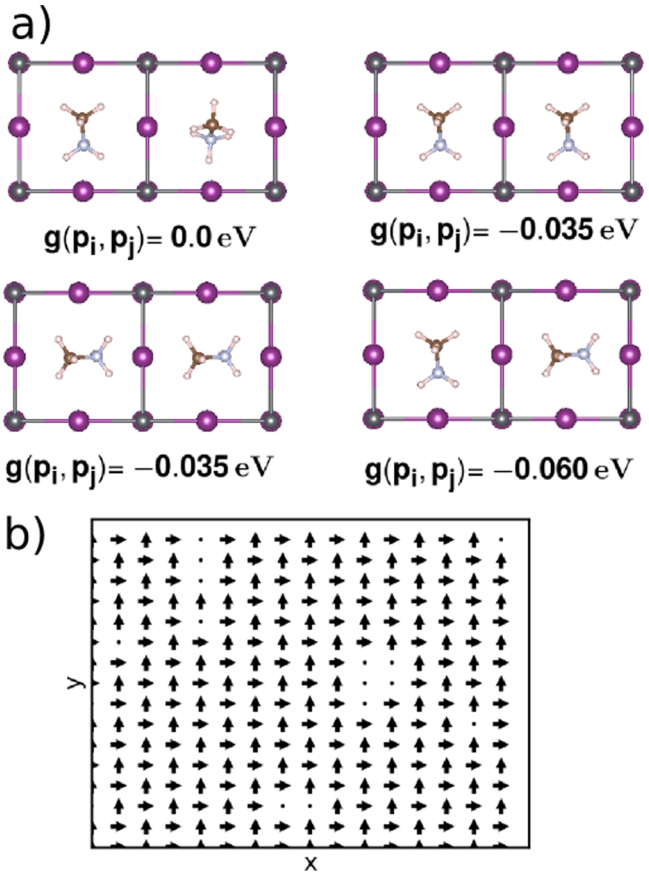

Figure 4. (a) Short-range coupling configurations used in Monte Carlo model Hamiltonian. Short-range coupling energies (see text) are given relative to the configuration at the upper left. The lower right configuration, corresponding to a "crossed" 90° arrangement of molecules, has the lowest (most favorable) short-range coupling energy. (b) Snapshot of molecular dipole orientations in an equilibrated Monte Carlo simulation, showing a majority of dipoles in a "crossed" configuration. Arrows denote orientations of molecules. Simulation temperature of this snapshot was 240 K.

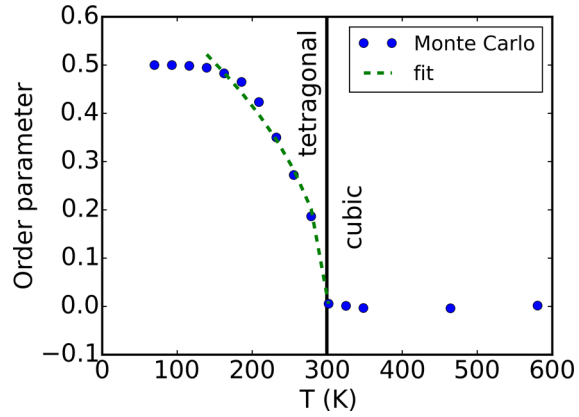

Figure 5. Order parameter as a function of temperature for the Monte Carlo simulation, showing phase transition between tetragonal and cubic phases. See text for definition of order parameter. Dots indicate the value of order parameter calculated from Monte Carlo simulations equilibrated at different temperatures. Dashed line indicates a fit of Monte Carlo data to the functional form $(T_c - T)^{2\beta}$ for the data below the transition temperature T_c.

within a thermodynamically accessible energy range. The LR interactions are described by dipole−dipole coupling.[13] Because our first-principles and model Hamiltonian calculations are performed within periodic boundary conditions, the dipole sum is evaluated using the Ewald summation technique.

We parametrize our effective Hamiltonian (eq 1) by performing a least-squares fit to first-principles energies, finding a root mean squared error of 7 meV per unit cell. In fitting eq 1, we take $\vec{p}_i$ to be the unit vector along the C−N direction and absorb the dipole magnitude and dielectric function into the fitting parameter K, which has the best-fit value of 4.5 eV Å^3. We find that the energetically most favorable SR coupling configuration of two adjacent molecules is one of the crossed arrangements, with one of the molecules pointed toward the other and the other at 90° (Figure 4a). This indicates that the SR interaction between MA molecules is considerably more complex than a dipole−dipole interaction, which would favor either a head-to-tail or an antiferroelectric orientation.

We proceed to extend our effective Hamiltonian to simulations on larger system sizes, with the aim of better understanding the tetragonal phase and its phase transitions by examining the molecular orientation distribution. Ab initio molecular dynamics simulations are computationally expensive and are limited in accuracy, for small unit cells, by spurious interactions between periodic images.[20] On the other hand, force field molecular dynamics (FFMD) developed for $MAPbI_3$ may not fully capture the nuances of hydrogen bonding. For instance, FFMD correctly describes a low-temperature phase transition from the orthorhombic phase but does not show any signs of a tetragonal−cubic phase transition.[17] Therefore, Monte Carlo simulations based on this effective Hamiltonian allow extraction of the molecular orientation correlations on a much larger spatial scale, while at the same time maintaining the fidelity of intermolecular interactions.

Upon running Monte Carlo simulations of this effective model over a temperature range of 70−600 K, we observe the formation of an ordered state below 300 K and a disordered state above 300 K (Figure 5). We use a 16 × 16 × 16 simulation cell for all temperatures, applying the Metropolis algorithm with acceptance ratio $\exp(-\Delta E/T)$, where ΔE is the change in energy between two simulation steps and T the simulation temperature. We find that 2×10^6 steps were sufficient for convergence of the ground state. In the disordered state, we find a random and isotropic distribution of molecular orientations, which we assign to the cubic phase, in light of the nearly isotropic cubic phase molecular orientations measured by neutron powder diffraction.[14] In the ordered state, there is bidirectional ordering of the molecules within the $(x-y)$ plane,[37] with a small number of isolated clusters oriented along z (Figure 4b). Through the process of hydrogen bonding, the molecules oriented in the $x-y$ plane induce displacement of iodines within this plane. The resulting I_6 octahedral rotations and distortions in this plane lead to reduced lattice constants in the x and y directions compared to the z direction, an effect which has been seen in molecular dynamics.[37] Therefore, given the tetragonal symmetry and the expected reduction in equatorial $(x-y)$ lattice constants, we assign this ordered phase in our Monte Carlo simulations as the room-temperature tetragonal phase of $MAPbI_3$. The simulated phase transition temperature is close to the experimental tetragonal−cubic transition temperature of 327 K.[14,53,54]

DOI: 10.1021/acsenergylett.7b00159
ACS Energy Lett. 2017, 2, 937−942

To investigate the phase transition in more detail, we define an order parameter that captures this kind of ordering. Defining f_i as the fraction of molecular dipoles aligned along Cartesian direction i, we take the order parameter $\sigma_i = \sqrt{f_1 f_2 f_3 / f_i} - f_i$. This is a measure of the number of molecules oriented perpendicular to direction i relative to the number parallel to direction i. That is, it is a proxy for the amount of tetragonal strain in the system, taking values 0.5 for pure bidirectional ordering, 0 for complete disorder, and −1 for unidirectional ordering. Fitting the dependence of σ_3 on temperature to the form $(T_c - T)^{2\beta}$, we find a critical exponent $\beta = 0.244$. This is consistent with the values of $\beta \approx 0.25$ reported for the tetragonal strain temperature dependence in a recent experiment.[55] In going from the cubic to the tetragonal phase, this model predicts a reduction in molar entropy of $R \ln 3$, as each molecule is constrained to a single Cartesian direction instead of all three. This reduction in entropy is consistent with $R \ln 3.2$ measured in experiments.[56]

In conclusion, we have shown that a small number of structural rules drive the structural behavior of $MAPbI_3$, and these can be understood as a trade-off between energetically favorable distortions of the inorganic lattice and hydrogen bonding modes constrained by the geometry of the MA molecule. Moreover, it is these rules, such as the predominance of crossed molecular orientations, which drive phase transitions and determine structural properties. These nondipolar interactions are as important as the electrostatic dipole−dipole interactions between molecules. The consequences of such emergent interactions on the excited state and electronic degrees of freedom will be left as a topic for future study.

AUTHOR INFORMATION

Corresponding Author

*E-mail: rappe@sas.upenn.edu.

ORCID

Liang Z. Tan: 0000-0003-4724-6369

Andrew M. Rappe: 0000-0003-4620-6496

Notes

The authors declare no competing financial interest.

ACKNOWLEDGMENTS

L.Z.T. was supported by the U.S. ONR under Grant N00014-14-1-0761. A.M.R. was supported by the U.S. ONR under Grant N00014-14-1-0761. Computational support was provided by the U.S. DOD through a Challenge Grant from the HPCMO and by the U.S. DOE through computer time at NERSC.

REFERENCES

(1) Zhou, H.; Chen, Q.; Li, G.; Luo, S.; Song, T.-B.; Duan, H.-S.; Hong, Z.; You, J.; Liu, Y.; Yang, Y. Interface engineering of highly efficient perovskite solar cells. *Science* **2014**, *345*, 542−546.

(2) Jeon, N. J.; Lee, H. G.; Kim, Y. C.; Seo, J.; Noh, J. H.; Lee, J.; Seok, S. I. o-Methoxy Substituents in Spiro-OMeTAD for Efficient Inorganic-Organic Hybrid Perovskite Solar Cells. *J. Am. Chem. Soc.* **2014**, *136*, 7837−7840.

(3) NREL. Renewable Electricity Futures Study. http://www.nrel.gov/analysis/re_futures/, 2015.

(4) Xing, G.; Mathews, N.; Sun, S.; Lim, S. S.; Lam, Y. M.; Grätzel, M.; Mhaisalkar, S.; Sum, T. C. Long-Range Balanced Electron- and Hole-Transport Lengths in Organic-Inorganic $CH_3NH_3PbI_3$. *Science* **2013**, *342*, 344−347.

(5) Stranks, S. D.; Eperon, G. E.; Grancini, G.; Menelaou, C.; Alcocer, M. J. P.; Leijtens, T.; Herz, L. M.; Petrozza, A.; Snaith, H. J. Electron-Hole Diffusion Lengths Exceeding 1 Micrometer in an Organometal Trihalide Perovskite Absorber. *Science* **2013**, *342*, 341−344.

(6) Wehrenfennig, C.; Eperon, G. E.; Johnston, M. B.; Snaith, H. J.; Herz, L. M. High Charge Carrier Mobilities and Lifetimes in Organolead Trihalide Perovskites. *Adv. Mater.* **2014**, *26*, 1584−1589.

(7) Umari, P.; Mosconi, E.; De Angelis, F. Relativistic GW calculations on $CH_3NH_3PbI_3$ and $CH_3NH_3SnI_3$ Perovskites for Solar Cell Applications. *Sci. Rep.* **2014**, *4*, 4467.

(8) Ogomi, Y.; Morita, A.; Tsukamoto, S.; Saitho, T.; Fujikawa, N.; Shen, Q.; Toyoda, T.; Yoshino, K.; Pandey, S. S.; Ma, T.; Hayase, S. $CH_3NH_3Sn_xPb_{(1-x)}I_3$ Perovskite Solar Cells Covering up to 1060 nm. *J. Phys. Chem. Lett.* **2014**, *5*, 1004−1011.

(9) Stoumpos, C. C.; Malliakas, C. D.; Kanatzidis, M. G. Semiconducting Tin and Lead Iodide Perovskites with Organic Cations: Phase Transitions, High Mobilities, and Near-Infrared Photoluminescent Properties. *Inorg. Chem.* **2013**, *52*, 9019−9038.

(10) Mosconi, E.; Quarti, C.; Ivanovska, T.; Ruani, G.; De Angelis, F. Structural and electronic properties of organo-halide lead perovskites: a combined IR-spectroscopy and ab initio molecular dynamics investigation. *Phys. Chem. Chem. Phys.* **2014**, *16*, 16137−16144.

(11) Filip, M. R.; Giustino, F. GW quasiparticle band gap of the hybrid organic-inorganic perovskite $CH_3NH_3PbI_3$: Effect of spin-orbit interaction, semicore electrons, and self-consistency. *Phys. Rev. B: Condens. Matter Mater. Phys.* **2014**, *90*, 245145.

(12) Poglitsch, A.; Weber, D. Dynamic disorder in methylammoniumtrihalogenoplumbates (II) observed by millimeter-wave spectroscopy. *J. Chem. Phys.* **1987**, *87*, 6373−6378.

(13) Leguy, A. M. A.; Frost, J. M.; McMahon, A. P.; Sakai, V. G.; Kochelmann, W.; Law, C.; Li, X.; Foglia, F.; Walsh, A.; O'Regan, B. C.; Nelson, J.; Cabral, J. T.; Barnes, P. R. F. The dynamics of methylammonium ions in hybrid organic-inorganic perovskite solar cells. *Nat. Commun.* **2015**, *6*, 7124.

(14) Weller, M. T.; Weber, O. J.; Henry, P. F.; Di Pumpo, A. M.; Hansen, T. C. Complete structure and cation orientation in the perovskite photovoltaic methylammonium lead iodide between 100 and 352 K. *Chem. Commun.* **2015**, *51*, 4180−4183.

(15) Yaffe, O.; et al. Local Polar Fluctuations in Lead Halide Perovskite Crystals. *Phys. Rev. Lett.* **2017**, *118*, 136001.

(16) Beecher, A. N.; Semonin, O. E.; Skelton, J. M.; Frost, J. M.; Terban, M. W.; Zhai, H.; Alatas, A.; Owen, J. S.; Walsh, A.; Billinge, S. J. Direct Observation of Dynamic Symmetry Breaking above Room Temperature in Methylammonium Lead Iodide Perovskite. *ACS Energy Letters* **2016**, *1*, 880−887.

(17) Mattoni, A.; Filippetti, A.; Saba, M. I.; Delugas, P. Methylammonium Rotational Dynamics in Lead Halide Perovskite by Classical Molecular Dynamics: The Role of Temperature. *J. Phys. Chem. C* **2015**, *119*, 17421−17428.

(18) Quarti, C.; Mosconi, E.; De Angelis, F. Structural and electronic properties of organo-halide hybrid perovskites from ab initio molecular dynamics. *Phys. Chem. Chem. Phys.* **2015**, *17*, 9394−9409.

(19) Carignano, M. A.; Kachmar, A.; Hutter, J. Thermal Effects on $CH_3NH_3PbI_3$ Perovskite from Ab Initio Molecular Dynamics Simulations. *J. Phys. Chem. C* **2015**, *119*, 8991−8997.

(20) Goehry, C.; Nemnes, G. A.; Manolescu, A. Collective Behavior of Molecular Dipoles in $CH_3NH_3PbI_3$. *J. Phys. Chem. C* **2015**, *119*, 19674−19680.

(21) Even, J.; Carignano, M.; Katan, C. Molecular disorder and translation/rotation coupling in the plastic crystal phase of hybrid perovskites. *Nanoscale* **2016**, *8*, 6222−6236.

(22) Amat, A.; Mosconi, E.; Ronca, E.; Quarti, C.; Umari, P.; Nazeeruddin, M. K.; Grätzel, M.; De Angelis, F. Cation-Induced Band-Gap Tuning in Organohalide Perovskites: Interplay of Spin-Orbit Coupling and Octahedra Tilting. *Nano Lett.* **2014**, *14*, 3608−3616.

(23) Liu, S.; Zheng, F.; Koocher, N. Z.; Takenaka, H.; Wang, F.; Rappe, A. M. Ferroelectric domain wall induced band gap reduction

DOI: 10.1021/acsenergylett.7b00159
ACS Energy Lett. 2017, 2, 937−942

and charge separation in organometal halide perovskites. *J. Phys. Chem. Lett.* **2015**, *6*, 693−699.
(24) Brivio, F.; Walker, A. B.; Walsh, A. Structural and electronic properties of hybrid perovskites for high-efficiency thin-film photovoltaics from first-principles. *APL Mater.* **2013**, *1*, 042111.
(25) Kim, M.; Im, J.; Freeman, A. J.; Ihm, J.; Jin, H. Switchable $S = 1/2$ and $J = 1/2$ Rashba bands in ferroelectric halide perovskites. *Proc. Natl. Acad. Sci. U. S. A.* **2014**, *111*, 6900−6904.
(26) Stroppa, A.; Di Sante, D.; Barone, P.; Bokdam, M.; Kresse, G.; Franchini, C.; Whangbo, M.-H.; Picozzi, S. Tunable ferroelectric polarization and its interplay with spin-orbit coupling in tin iodide perovskites. *Nat. Commun.* **2014**, *5*, 5900.
(27) Even, J.; Pedesseau, L.; Jancu, J.-M.; Katan, C. Importance of Spin-Orbit Coupling in Hybrid Organic/Inorganic Perovskites for Photovoltaic Applications. *J. Phys. Chem. Lett.* **2013**, *4*, 2999−3005.
(28) Kepenekian, M.; Robles, R.; Katan, C.; Sapori, D.; Pedesseau, L.; Even, J. Rashba and Dresselhaus Effects in Hybrid Organic-Inorganic Perovskites: From Basics to Devices. *ACS Nano* **2015**, *9*, 11557−11567.
(29) Zheng, F.; Tan, L. Z.; Liu, S.; Rappe, A. M. Rashba spin−orbit coupling enhanced carrier lifetime in $CH_3NH_3PbI_3$. *Nano Lett.* **2015**, *15*, 7794−7800.
(30) Azarhoosh, P.; Frost, J. M.; McKechnie, S.; Walsh, A.; van Schilfgaarde, M. Relativistic origin of slow electron-hole recombination in hybrid halide perovskite solar cells. 2016, *arXiv:1604.04500*.
(31) Etienne, T.; Mosconi, E.; De Angelis, F. Dynamical Origin of the Rashba Effect in Organohalide Lead Perovskites: A Key to Suppressed Carrier Recombination in Perovskite Solar Cells? *J. Phys. Chem. Lett.* **2016**, *7*, 1638−1645.
(32) Leppert, L.; Reyes-Lillo, S. E.; Neaton, J. B. Electric Field- and Strain-Induced Rashba Effect in Hybrid Halide Perovskites. *J. Phys. Chem. Lett.* **2016**, *7*, 3683−3689.
(33) Grancini, G.; Srimath Kandada, A. R.; Frost, J. M.; Barker, A. J.; De Bastiani, M.; Gandini, M.; Marras, S.; Lanzani, G.; Walsh, A.; Petrozza, A. Role of microstructure in the electron-hole interaction of hybrid lead halide perovskites. *Nat. Photonics* **2015**, *9*, 695−701.
(34) Ma, J.; Wang, L.-W. Nanoscale Charge Localization Induced by Random Orientations of Organic Molecules in Hybrid Perovskite $CH_3NH_3PbI_3$. *Nano Lett.* **2015**, *15*, 248−253.
(35) Frost, J. M.; Butler, K. T.; Walsh, A. Molecular ferroelectric contributions to anomalous hysteresis in hybrid perovskite solar cells. *APL Mater.* **2014**, *2*, 081506.
(36) Fan, Z.; Xiao, J.; Sun, K.; Chen, L.; Hu, Y.; Ouyang, J.; Ong, K. P.; Zeng, K.; Wang, J. Ferroelectricity of $CH_3NH_3PbI_3$ Perovskite. *J. Phys. Chem. Lett.* **2015**, *6*, 1155−1161.
(37) Deretzis, I.; Di Mauro, B. N.; Alberti, A.; Pellegrino, G.; Smecca, E.; La Magna, A. Spontaneous bidirectional ordering of $CH_3NH_3^+$ in lead iodide perovskites at room temperature: The origins of the tetragonal phase. *Sci. Rep.* **2016**, *6*, 24443.
(38) Rabe, K. M.; Waghmare, U. V. First-principles model Hamiltonians for ferroelectric phase transitions. *Ferroelectrics* **1992**, *136*, 147.
(39) Rabe, K. M.; Waghmare, U. V. Ferroelectric phase transitions from first principles. *J. Phys. Chem. Solids* **1996**, *57*, 1397−1403.
(40) Stroppa, A.; Quarti, C.; De Angelis, F.; Picozzi, S. Ferroelectric Polarization of $CH_3NH_3PbI_3$: A Detailed Study Based on Density Functional Theory and Symmetry Mode Analysis. *J. Phys. Chem. Lett.* **2015**, *6*, 2223−2231.
(41) Quarti, C.; Mosconi, E.; De Angelis, F. Interplay of Orientational Order and Electronic Structure in Methylammonium Lead Iodide: Implications for Solar Cell Operation. *Chem. Mater.* **2014**, *26*, 6557−6569.
(42) Frost, J. M.; Butler, K. T.; Brivio, F.; Hendon, C. H.; van Schilfgaarde, M.; Walsh, A. Atomistic Origins of High-Performance in Hybrid Halide Perovskite Solar Cells. *Nano Lett.* **2014**, *14*, 2584−2590.
(43) Motta, C.; El-Mellouhi, F.; Kais, S.; Tabet, N.; Alharbi, F.; Sanvito, S. Revealing the role of organic cations in hybrid halide perovskite $CH_3NH_3PbI_3$. *Nat. Commun.* **2015**, *6*, 7026.
(44) Perdew, J. P.; Burke, K.; Ernzerhof, M. Generalized Gradient Approximation Made Simple. *Phys. Rev. Lett.* **1996**, *77*, 3865.
(45) Tkatchenko, A.; Scheffler, M. Accurate molecular van der Waals interactions from ground-state electron density and free-atom reference data. *Phys. Rev. Lett.* **2009**, *102*, 073005.
(46) Egger, D. A.; Kronik, L. Role of Dispersive Interactions in Determining Structural Properties of Organic-Inorganic Halide Perovskites: Insights from First-Principles Calculations. *J. Phys. Chem. Lett.* **2014**, *5*, 2728−2733.
(47) Rappe, A. M.; Rabe, K. M.; Kaxiras, E.; Joannopoulos, J. D. Optimized Pseudopotentials. *Phys. Rev. B: Condens. Matter Mater. Phys.* **1990**, *41*, 1227−1230.
(48) Ramer, N. J.; Rappe, A. M. Designed Nonlocal Pseudopotentials for Enhanced Transferability. *Phys. Rev. B: Condens. Matter Mater. Phys.* **1999**, *59*, 12471−12478.
(49) Kawamura, Y.; Mashiyama, H.; Hasebe, K. Structural Study on Cubic-Tetragonal Transition of $CH_3NH_3PbI_3$. *J. Phys. Soc. Jpn.* **2002**, *71*, 1694−1697.
(50) Ong, K. P.; Goh, T. W.; Xu, Q.; Huan, A. Mechanical Origin of the Structural Phase Transition in Methylammonium Lead Iodide $CH_3NH_3PbI_3$. *J. Phys. Chem. Lett.* **2015**, *6*, 681−685.
(51) Lee, J. H.; Lee, J.-H.; Kong, E.-H.; Jang, H. M. Two Distinct Modes of Hydrogen-Bonding Interaction in the Prototypic Hybrid Halide Perovskite, Tetragonal $CH_3NH_3PbI_3$. 2015,*arXiv:1511.02643*.
(52) Glazer, A. M. The Classification of Tilted Octahedra in Perovskites. *Acta Crystallogr., Sect. B: Struct. Crystallogr. Cryst. Chem.* **1972**, *28*, 3384−92.
(53) Baikie, T.; Fang, Y.; Kadro, J. M.; Schreyer, M.; Wei, F.; Mhaisalkar, S. G.; Grätzel, M.; White, T. J. Synthesis and Crystal Chemistry of the Hybrid Perovskite $CH_3NH_3PbI_3$ for Solid-State Sensitised Solar Cell Applications. *J. Mater. Chem. A* **2013**, *1*, 5628−5641.
(54) Schelhas, L. T.; Christians, J. A.; Berry, J. J.; Toney, M. F.; Tassone, C. J.; Luther, J. M.; Stone, K. H. Monitoring a Silent Phase Transition in $CH_3NH_3PbI_3$ Solar Cells via Operando X-ray Diffraction. *ACS Energy Letters* **2016**, *1*, 1007−1012.
(55) Comin, R.; Crawford, M. K.; Said, A. H.; Herron, N.; Guise, W. E.; Wang, X.; Whitfield, P. S.; Jain, A.; Gong, X.; McGaughey, A. J. H.; Sargent, E. H. Lattice dynamics and the nature of structural transitions in organolead halide perovskites. *Phys. Rev. B: Condens. Matter Mater. Phys.* **2016**, *94*, 094301.
(56) Onoda-Yamamuro, N.; Matsuo, T.; Suga, H. Calorimetric and IR spectroscopic studies of phase transitions in methylammonium trihalogenoplumbates (II). *J. Phys. Chem. Solids* **1990**, *51*, 1383−1395.

DOI: 10.1021/acsenergylett.7b00159
ACS Energy Lett. 2017, 2, 937−942